




## Fast crystal growth of ice VII owing to the decoupling of translational and rotational ordering

Xuan Zhang <sup>1,4</sup>, Yifeng Yao<sup>1,4</sup>, Hongyi Li<sup>2</sup>, Andre Python <sup>2,3</sup>✉ & Kenji Mochizuki <sup>1</sup>✉

Despite the abundance of water's crystalline polymorphs, the growth mechanisms of most ice forms remain poorly understood. This study applies extensive molecular dynamics (MD) simulations to examine the growth of ice VII, revealing a fast growth rate comparable to pure metals while maintaining robust hydrogen-bond networks. The results from an unsupervised machine learning applied to identify local structure suggest that the surface of ice VII consistently exhibits a body-centered cubic (bcc) plastic ice layer, indicating the decoupling of translational and rotational orderings. The study also uncovers the ultrafast growth rate of pure plastic ice, indicating that orientational disorder in the crystal structure may be associated with faster kinetics. Additionally, we discuss the impacts of interfacial plastic layer width and surface roughness on growth mode.

<sup>1</sup>Department of Chemistry, Zhejiang University, 310012 Hangzhou, P. R. China. <sup>2</sup>School of Mathematical Sciences, Zhejiang University, 310012 Hangzhou, P. R. China. <sup>3</sup>Center for Data Science, Zhejiang University, 310012 Hangzhou, P. R. China. <sup>4</sup>These authors contributed equally: Xuan Zhang, Yifeng Yao. ✉email: [apython@zju.edu.cn](mailto:apython@zju.edu.cn); [kenji\\_mochizuki@zju.edu.cn](mailto:kenji_mochizuki@zju.edu.cn)

Fast crystal growth and the underlying molecular mechanisms have gained considerable attention in condensed matter physics and materials science<sup>1,2</sup>. Water crystals display remarkable polymorphism, with experimental evidence supporting the presence of twenty unique ice forms thus far<sup>3–6</sup>. Moreover, simulations anticipate the discovery of additional distinct ice structures<sup>7,8</sup>. Despite the large variety in hydrogen-bond networks observed in different ice forms<sup>9</sup>, little attention has been paid to the potential variations in growth mode and rate.

The growth rate of ordinary ices, ice Ih and ice Ic, is relatively slow, with a maximum rate of 0.1 m/s<sup>10–12</sup>. By contrast, numerous dynamic compression experiments have identified rapid formation of ice VII on a sub-microsecond time scale, implying that either the nucleation, the melt growth, or both processes are fast<sup>13–16</sup>. Ice VII has a body-centred cubic oxygen arrangement with two interpenetrating hydrogen-bond networks. One of the sub-networks is identical to that of ice Ic, indicating that both ice VII and ice I (Ih and Ic) share robust hydrogen-bond networks. The question of whether ice VII can form significantly faster than ice I, along with the molecular mechanisms associated with this difference, remains a topic of great interest. However, the growth kinetics of ice VII are still not well understood, primarily due to the challenges of directly accessing the melt growth process via an interface between two condensed phases in experiments, especially under high-pressure conditions.

In general, when the temperature  $T$  is controlled to be uniform in space, the intrinsic normal growth rate  $V_n$  is expressed as the product of a kinetic factor  $K(T)$  and a thermodynamic term:

$$V_n(T) = K(T) \times [1 - \exp(-\Delta\mu/k_B T)], \quad (1)$$

where  $\Delta\mu = \mu_{\text{liq}} - \mu_{\text{cry}}$  is the difference between the chemical potentials of the crystal and liquid, and  $k_B$  is the Boltzmann constant. The thermodynamic term arises from the gain of free energy during crystallisation, whereas the kinetic factor represents the rate of addition of atoms to the crystal surface. Unlike the thermodynamic term, the kinetic factor has been the subject of intense discussion<sup>1,2,17–19</sup>.

The Wilson–Frenkel (WF) model predicts that the kinetic factor is governed by the self-diffusion coefficient  $D$  in the melt<sup>17,20,21</sup>:

$$K^{\text{wf}}(T) = \frac{6dDf}{\lambda^2} e^{-\Delta s/k_B}, \quad (2)$$

where  $d$  is the interplanar distance,  $\lambda$  is the displacement length associated with  $D$ ,  $\Delta s$  is the entropy of the liquid with respect to that of the crystal, and  $f$  is the fraction of the growth sites.  $\ln D$  is proportional to the activation energy for diffusion ( $E_d$ ), as  $\ln D \propto -E_d/k_B T$ . The consideration of interfacial energy owing to preordering may refine the prediction<sup>19</sup>. Although the WF model may fail to predict the absolute value, the overall temperature dependence of the growth rate for organic and inorganic molecules<sup>22</sup>, metallic alloys<sup>19</sup>, silicon<sup>23</sup>, and hexagonal ice<sup>24</sup> (except faceted surfaces under low supercooling<sup>25</sup>) is reasonably well described by the diffusion-controlled scenario, in which  $K(T)$  is strongly depressed upon cooling owing to reduced diffusivity.

By contrast, the growth rate of some materials does not drop even under high supercooling, suggesting a barrierless ordering<sup>1,2</sup>. An apparent turnover of the growth rate was predicted for pure metals at  $\sim 0.7T_m$  (where  $T_m$  is the melting temperature)<sup>26</sup>, but it was later confirmed to be a consequence of the instability limit of the supercooled liquid, below which a number of homogeneous nucleations occur simultaneously throughout the liquid<sup>2</sup>. The collision-controlled model treats crystallisation as wave propagation, in which the ordering simultaneously proceeds in many surface layers rather than at a sharp crystal–liquid interface. In this case,  $K(T) \propto \sqrt{3k_B T/m}$ , where  $m$  is the particle mass<sup>18,27</sup>.

Harrowell et al. recently demonstrated that the WF model can describe a barrierless growth when the activation energy for crystallisation ( $E_a$ ) is applied instead of  $E_d$ , and the ratio of  $E_a/E_d$  is smaller than 0.25<sup>2,28</sup>. The molecular mechanism of barrierless growth has been attributed to a less frustrated solid–liquid interface, which enables liquid to crystallise through a small adjustment via preordering<sup>1</sup> or an interfacial liquid with a crystalline ground state<sup>2,28</sup>. In addition to the unique temperature dependence, the barrierless ordering, which involves crossing little to no activation barrier, results in an anomalous growth rate ( $>10^2$  m/s for monoatomic metals)<sup>2,29</sup>.

Globular molecules, which have isotropic interactions, such as monoatomic metals and colloids, tend to exhibit faster growth rates than orientationally ordered crystals<sup>1,2,19</sup>. Although ice polymorphs, including ice VII (proton disordered, but possible orientations are limited), are categorised into the latter group, the only exception may be plastic ice crystals, in which water molecules nearly freely rotate at their lattice sites and behave like globular molecules<sup>30–32</sup>.

Here, we perform molecular dynamics (MD) simulations of the crystal–liquid coexistence of ice Ih and two bcc-forming ice crystals (ice VII and plastic ice) and bring evidence that ice VII and plastic ice grow much faster than ice Ih. An unsupervised machine-learning (UML) technique suggests the presence of an interfacial plastic layer between ice VII and liquid, which does not appear on the ice Ih surface. We conclude that the decoupling of translational and rotational ordering, combined with the change in surface roughness and interface width, is associated with the unique growth mode of ice VII.

## Results

**Growth rate.** Figure 1a–c present the schematic descriptions of ice Ih, ice VII, and plastic ice. A comparison of Fig. 1b, c reveals that oxygen atoms in ice VII and plastic ice have bcc lattice arrangements (see molecules in lime). A water molecule in ice VII forms four hydrogen bonds with its neighbours and the possible orientation of water dipole vector is limited, whereas water molecules in plastic ice rotate freely. We first compute the growth rate of those ice crystals in the classical WF model ( $V_n^{\text{wf}}$ ) from Eqs. (1) and (2) combined with  $\Delta\mu = (T_m - T)\Delta h_m/T_m$ , where  $\Delta h_m$  is the enthalpy of fusion at the melting temperature  $T_m$ . Table 1 summarises the physical quantities constituting Eq. (2). The fraction of favourable growth sites  $f$  is not precisely determined; it is likely within the range of 1/4 and 1<sup>17,23,29</sup>. We here suppose that  $f=1.0$ .  $\Delta s$  is approximated by  $\Delta h_m/T_m$ . The displacement length  $\lambda$  is taken from the effective molecular radius<sup>33</sup>, although  $\lambda$  can be an actual displacement that is slightly shorter than the radius of a molecule<sup>28</sup>. As shown in the inset of Fig. 1d, the results of the WF model suggest that the growth rate of ice Ih is the lowest, whereas plastic ice exhibits the highest growth rate. The difference predominantly arises from the entropy change during crystallisation.

Figure 1d–f plot the growth rate  $V_n$  measured in MD simulations for an elongated crystal–liquid system. The melt growth dynamics are seen in Supplementary Movie 1.  $V_n$  is computed from Eq. (4) and a linear fitting to the time evolution of ice-like molecules (Supplementary Fig. 2). Upon cooling from  $T_m$ , liquid water exhibits a glass transition at 4.8 GPa, and plastic ice transitions to ice VII at 10.5 GPa (Supplementary Fig. 3). In the current research, although the crystallisation of high-pressure ices from glassy water represents a captivating subject matter<sup>34</sup>, we have chosen not to delve into this particular topic. As a consequence, the coexistence between ice VII and liquid water persists in  $0.80 < T/T_m$  at 4.8 GPa, and that between plastic ice and liquid water persists in  $0.75 < T/T_m$  at 10.5 GPa.

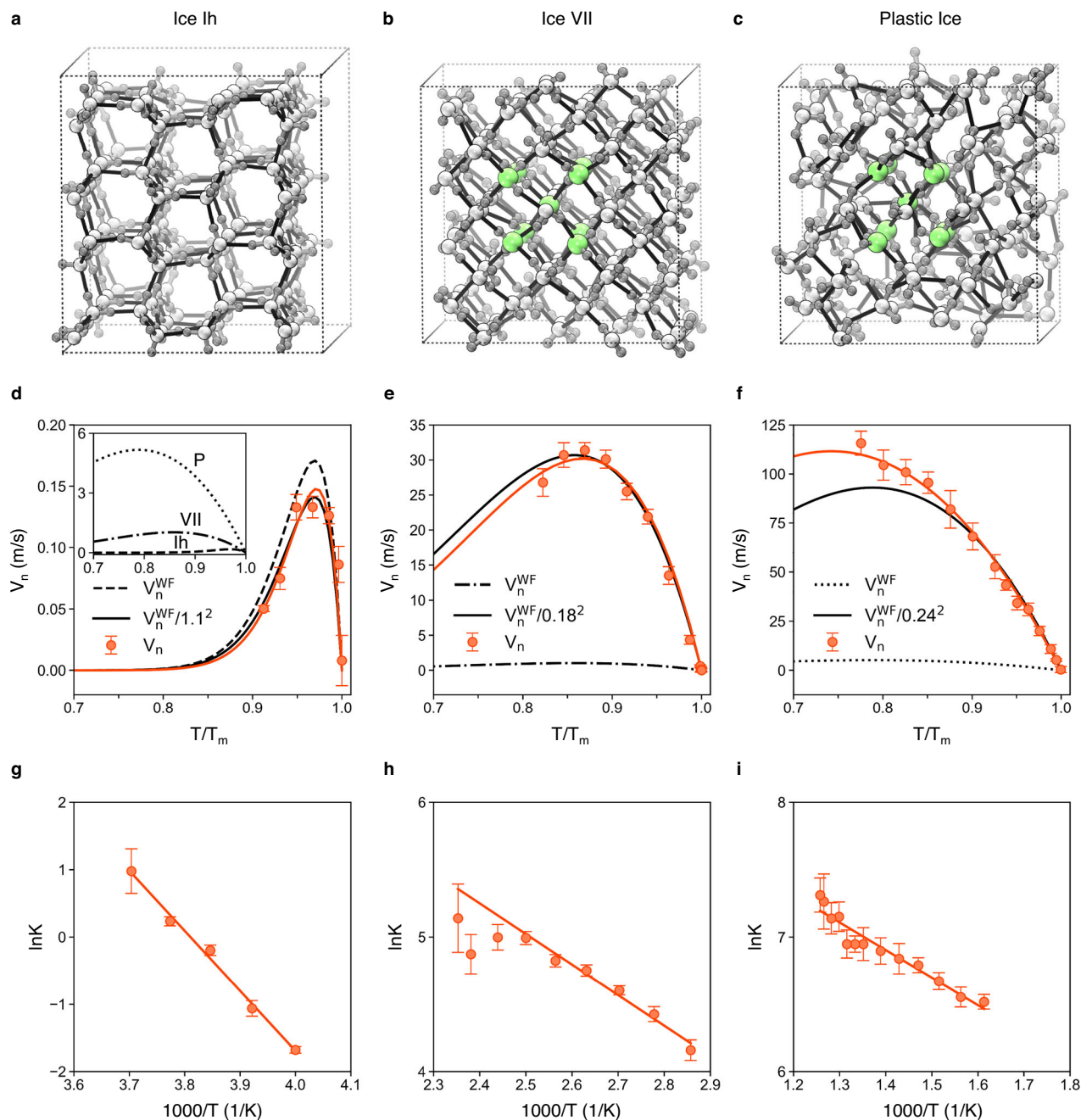


**Fig. 1** Various melt growth modes observed for three different ice forms. **a-c** Schematic descriptions of crystal structures. In **(a)**, the primary prismatic surface of ice Ih is oriented toward the top. In **(b)** and **(c)**, the side, top, and front are all  $\{100\}$  surfaces of a bcc-lattice. Nine lime molecules represent a bcc-lattice. **d-f** The normal growth rate measured in molecular dynamics simulations ( $V_n$ ), the Wilson-Frenkel prediction ( $V_n^{WF}$ ), and the scaled  $V_n^{WF}$  for the best fit to  $V_n$ .  $T_m$  is the melting temperature of each ice crystal. The solid orange line is a fitting to  $V_n$  using the activation energy for crystallisation ( $E_a$ ). The inset of **(d)** compares  $V_n^{WF}$  for the three ice crystals. **g-i** The Arrhenius plot of the kinetic factor  $K(T)$  obtained from  $V_n$  and Eq. (1). The solid orange line represents a linear fitting ( $2.5 < 1000/T < 2.9$  is used for ice VII).

In Fig. 1d, the diffusion-controlled scenario is apparently identified for ice Ih, as previously reported<sup>10,24</sup>, in which  $V_n$  first increases and then decays toward zero upon cooling. As the best fit to  $V_n$  is achieved by a slight scaling ( $V_n^{WF}/1.1^2$ ), the absolute values and temperature dependence of the measured  $V_n$  are reasonably well predicted by the WF model.

Figure 1e demonstrates that  $V_n$  for ice VII also follows the diffusion-controlled scenario. However, the WF prediction seriously fails in describing the measured  $V_n$ , except for the maximum  $V_n$  temperature. In particular, ice VII grows 220 times faster than ice Ih, and reaches a maximum  $V_n$  of 31 m/s at

$T/T_m = 0.86$ , which is comparable to the fast growth rate observed for Pb and Ag (at  $T/T_m \sim 0.7$ ) with a barrierless mechanism<sup>2</sup>.

Figure 1f shows that  $V_n$  of plastic ice rises monotonically with cooling, unlike ice Ih and ice VII. The  $V_n$  eventually reaches 116 m/s at  $T/T_m = 0.75$ , which positions plastic ice in the category of materials with the highest growth rate<sup>29</sup>. Water molecules in plastic ice maintain bcc-oxygen arrangements, similar to ice VII, but they lose their distinct hydrogen-bond network and rotate nearly freely at lattice sites. It is not surprising that the nearly spherical nature of water molecules in the plastic phase facilitates

**Table 1** Quantities used in the Wilson-Frenkel prediction for ice Ih, ice VII, and plastic ice.

	$P$ (GPa)	Surface	$T_m$ (K)	$\Delta h_m$ (kJ/mol)	$d$ (nm)	$\lambda$ (nm)	$E_d$ (kJ/mol)	Max $V_n^{wf}$ (m/s)	$E_a$ (kJ/mol)	Max $V_n$ (m/s)
Ih	$10^{-4}$	Prism	274.0	7.5	0.38	0.14	72.1	0.18	74.2	0.14
VII	4.8	{100}	425.6	8.9	0.16	0.14	17.2	1.0	18.9	31
Plastic	10.5	{100}	799.3	4.3	0.16	0.14	22.7	5.2	17.1	116

$\Delta h_m$  is the enthalpy of fusion at the melting temperature  $T_m$ . The interplanar distance ( $d$ ) is obtained from configurations equilibrated at  $T_m$ . The displacement length ( $\lambda$ ) is defined as the effective radius of molecules, calculated as half of the intermolecular distance for the first peak in the oxygen-oxygen radial distribution function (Supplementary Fig. 1). The activation energies  $E_d$  and  $E_a$  for diffusion and crystallisation are obtained by linearly fitting the Arrhenius plot in Supplementary Fig. 3 and Fig. 1g–i, respectively. The maximum growth rate obtained from the Wilson-Frenkel model and molecular dynamics simulations are represented by  $\max V_n^{wf}$  and  $\max V_n$ , respectively.

the propagation of crystal front. However, unlike previous studies that compared growth patterns between different molecular species, this study presents the finding that the growth kinetics of an identical molecule is significantly accelerated by the presence of orientational disorder within the crystal structure.

The primary prismatic surface for ice Ih and {100} surface for the two bcc-forming ice crystals are chosen, but a similar temperature dependence is observed for the other surfaces (see literature for ice Ih<sup>10,24</sup> and Supplementary Fig. 4 for ice VII and plastic ice). By examining systems with a surface area four times larger, our results suggest that the growth rate is independent of the size of the interface area ( $N=49152$ );  $V_n$  of ice Ih, ice VII, and plastic ice is  $0.14 \pm 0.02$  m/s at  $0.97 T_m$ ,  $31 \pm 2$  m/s at  $0.85 T_m$ , and  $116 \pm 7$  m/s at  $0.78 T_m$ , respectively, for the current system (see Fig. 1d–f);  $0.10 \pm 0.01$ ,  $30 \pm 1$ , and  $111 \pm 2$  m/s for the quadruple system.

We also compute the kinetic factor  $K$  from  $V_n$  combined with Eq. (1). In Fig. 1g–i, the Arrhenius plot of  $K$  provides the activation energy for crystallisation ( $E_a$ ) within the generalised WF equation (Table 1). The resulting  $E_a$  values for ice Ih and ice VII are, respectively, comparable to the activation energy for self-diffusion ( $E_d$ ) in the melt, which agrees with the fact that the temperature dependence of the measured  $V_n$  overlaps well with the scaled  $V_n^{wf}$ . We later discuss why  $\ln K$  deviates from a linear function of  $1/T$  at high temperatures in the case of ice VII. Unlike ice Ih and ice VII,  $E_a$  for plastic ice is certainly lower than  $E_d$ , which shifts the  $V_n$  peak to a lower temperature than that of  $V_n^{wf}$ . The resulting  $E_a/E_d$  of 0.75 is still much larger than the threshold of 0.25 for a (nearly) barrierless growth mode<sup>2,28</sup>. Thus, if the plastic phase can be cooled below  $0.75T_m$  without the transition to ice VII, the  $V_n$  peak would be detectable, as suggested by the solid orange line in Fig. 1f. More importantly, we find that  $E_a$  for ice VII is almost equal to that of plastic ice, implying that the incorporation of liquid molecules into ice VII and plastic ice occurs via a similar ordering mechanism.

**Classification of local environments.** An intriguing phenomenon we encountered is that ice VII can grow much faster than ice Ih, even though in both cases the two ice crystals construct robust hydrogen-bond networks, unlike plastic ice. To autonomously characterise their local molecular environments on a single particle level, we employ the UML scheme that uses a neural network-based autoencoder combined with the Gaussian mixture model (GMM)<sup>35,36</sup>. Our descriptor for the  $j$ -th molecule is encoded into a 6-dimensional vector;  $\mathbf{Q}(j) = (\{\bar{q}_l(j)\})$ , where  $l$  is the positional symmetry of neighbours which can take the value 2, 4, 6, 8, 10, and 12<sup>37</sup>. A neural network is trained using two independent data sets; (i) the vectors  $\mathbf{Q}(j)$  from all the particles in crystal-liquid configurations at  $T/T_m=0.8, 0.9$ , and  $1.0$  for ice Ih; and (ii) those for the bcc-forming ice crystals (i.e., ice VII and plastic ice). To find the optimal dimensionality of the bottleneck layer, we evaluate the reconstruction of mean square errors (MSE) of the autoencoder with varying dimensionality<sup>38</sup>. In Fig. 2a, we detect the presence of an elbow when the number of

bottleneck nodes is equal to 3 (see L-method<sup>39</sup>) for both training sets. These results suggest that a three-dimensional nonlinear projection of the original input vectors is sufficient to preserve the relevant information. The relative importance (RI) of the input variables in neural network models refers to the degree to which each predictor contributes to the network output. To reduce the risk of bias in determining relative importance, we compare the results of two approaches, including the improved stepwise<sup>40</sup> and the input perturbation<sup>41</sup> methods. Both methods yielded results that concur in identifying that  $\bar{q}_1$  exhibits the largest variation in the training data (Supplementary Fig. 5). For ice Ih, the most relevant feature is  $\bar{q}_6$  with a RI of about 46% and the second is  $\bar{q}_4$  with RI of about 27%. For bcc-forming ice crystals, the most relevant features are  $\bar{q}_6$ , with a RI of about 54%, and  $\bar{q}_8$  with a RI of about 27%.

We then apply GMM in the respective three-dimension subspace and compute the Bayesian information criterion (BIC) for various numbers of Gaussian components in the mixture model. Figure 2b shows the presence of an elbow when the number of Gaussian components is equal to two for ice Ih. For the bcc-forming ice crystals, an elbow is observed when the number of Gaussian components is equal to three. Accordingly, the local molecular environment is classified into two relevant clusters for ice Ih and three for the bcc-forming ice crystals. Figure 2c shows how the original probability distributions for the bcc-forming ice crystals are decomposed into three Gaussian distributions on each axis in the determined subspace (named as  $\chi_1$ ,  $\chi_2$ , and  $\chi_3$ ).

In Fig. 3a–c, water molecules are coloured according to the type of cluster to which they belong. Figure 3a suggests that the coexistence between ice Ih and liquid is well-segregated into the ice domain (grey) and the liquid domain (blue). Their direct contact indicates that liquid water molecules directly incorporate into the ice Ih surface. By contrast, Fig. 3b shows that an interfacial domain (green) is present between ice VII (orange) and liquid (blue). Figure 3d illustrates that the density profile of the interfacial domain retains its layered structures, which are somewhat wider than those observed in ice VII. The thin interfacial layer is invariably detected between ice VII and liquid for all investigated temperatures. The thickness of the interfacial layer, although it fluctuates, is constant during the freezing of ice VII (see Supplementary Fig. 6 for details). Therefore, liquid water molecules necessarily transition to ice VII through the intermediate green layer.

Our approach identifies an intermediate layer even when we only provide the ice VII-liquid coexistence structures as input for UML, excluding the plastic ice-liquid coexistence structures (Supplementary Fig. 7).

Figure 3c shows that the coexistence of plastic ice and liquid is represented by two domains at  $T/T_m=0.8, 0.9$ , and  $1.0$ , similar to that for ice Ih. At these temperatures, liquid water molecules (blue) directly incorporate into plastic ice (green). When the temperature is further cooled to  $T/T_m=0.7$ —the phase boundary between ice VII and plastic ice is crossed—almost half of the crystal domain is identified as ice VII (orange). The crystal region is not fully covered by orange dots, because the small free energy

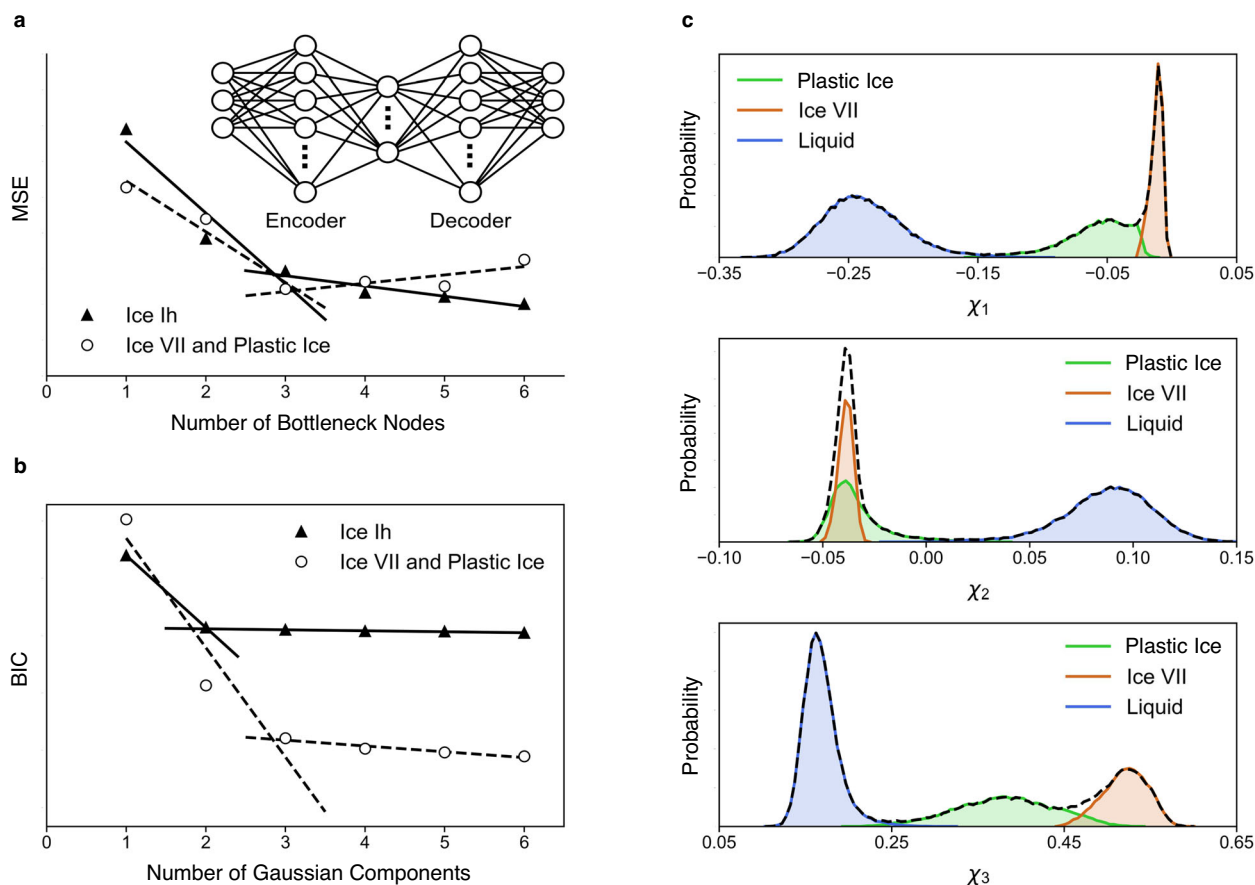


**Fig. 2 Classification of local molecular environments into relevant clusters, using the unsupervised machine learning approach for crystal-liquid coexistence systems.** **a** Mean square errors (MSE) of the autoencoder as a function of the number of bottleneck nodes. The inset describes the architecture of a neural-network-based autoencoder, which finds a low-dimensional representation of the input vectors  $\mathbf{Q}$ , from which the decoder reconstructs an approximation of the input as output  $\hat{\mathbf{Q}}$  while preserving the relevant information. **b** Bayesian information criterion (BIC) as a function of the number of Gaussian components in the Gaussian mixture model. **c** Probability distributions of three clusters found for the coexistence between liquid and bcc-forming ice crystals, projected onto each axis in the determined  $\chi_1$ - $\chi_2$ - $\chi_3$  subspace.

barrier between ice VII and plastic ice at this condition allows their incessant alternations<sup>42</sup>. Our results demonstrate that although oxygen atoms in ice VII and plastic ice both adopt a bcc arrangement, the distortion caused by the lack of specific hydrogen-bond networks is sufficiently large to distinguish plastic ice from ice VII if we choose an appropriate order parameter.

**Characterisation of the interfacial layer.** The clustering analysis suggests that the interfacial domain existing between ice VII and liquid possesses the same structural features as plastic ice (both coloured in green). In addition, we compare their dynamic features. Figure 3e, f show the reorientational correlation function (RCF)  $\langle \mathbf{u}_i(\Delta t + t_0) \cdot \mathbf{u}_i(t_0) \rangle$ , and the mean square displacement (MSD)  $\langle |\mathbf{r}_i(\Delta t + t_0) - \mathbf{r}_i(t_0)|^2 \rangle$  for water molecules belonging to three different domains in the ice VII-liquid configuration at  $T_m$ . Here,  $\mathbf{u}_i(t)$  represents the unit vector along the dipole direction, and  $\mathbf{r}_i(t)$  represents the oxygen position for the  $i$ -th molecule at time  $t$ ; the parentheses  $\langle \dots \rangle$  denote the ensemble average over the particles and over the reference time  $t_0$ . The particles are labelled based on their configuration at  $t_0$ . The results show that the RCF of the interfacial domain decays similarly to that of the liquid. However, the MSD for the interfacial domain resembles that of ice VII, rather than liquid. The non-zero slope in the MSD for the interfacial domain is attributed to the diffusion into the liquid region. Supplementary Fig. 8 shows the  $z$ -dependence of

the diffusion coefficient and the relaxation time. The observed facile rotational but less diffusional characteristics indicate a plastic phase. Therefore, the interfacial domain between ice VII and liquid is classified as a plastic crystal from both structural and dynamic perspectives.

The presence of such an intermediate wetting layer suggests that the surface tension (free energy) between ice VII and liquid is greater than the sum of the surface tensions between ice VII and plastic ice and between plastic ice and liquid, analogous to a quasi-liquid layer at the ice-vapour interface<sup>43</sup>. The appearance of a metastable plastic phase (not bcc-plastic) is also observed during the homogeneous nucleation of ice VII, which is in line with the Ostwald step rule<sup>8</sup>. However, because the arrangement of oxygen atoms in the metastable plastic ice differs from that in the final state (ice VII), both oxygen and hydrogen atoms must be simultaneously rearranged in the second step of homogeneous nucleation. In contrast, we underline that almost complete decoupling of translational and rotational ordering during crystallisation occurs in the melt growth of ice VII.

On-site observations describe how each molecule is absorbed onto the crystal surface. Even in cases of the first-order solidification, the molecular-level incorporation process can differ between materials due to their surface structure, and hence, affects the growth rate<sup>17,18,20,21,27</sup>. Figure 4a tracks the Voronoi volume of a typical water molecule at the instance when it incorporates into ice VII from liquid, together with the cluster identification. A

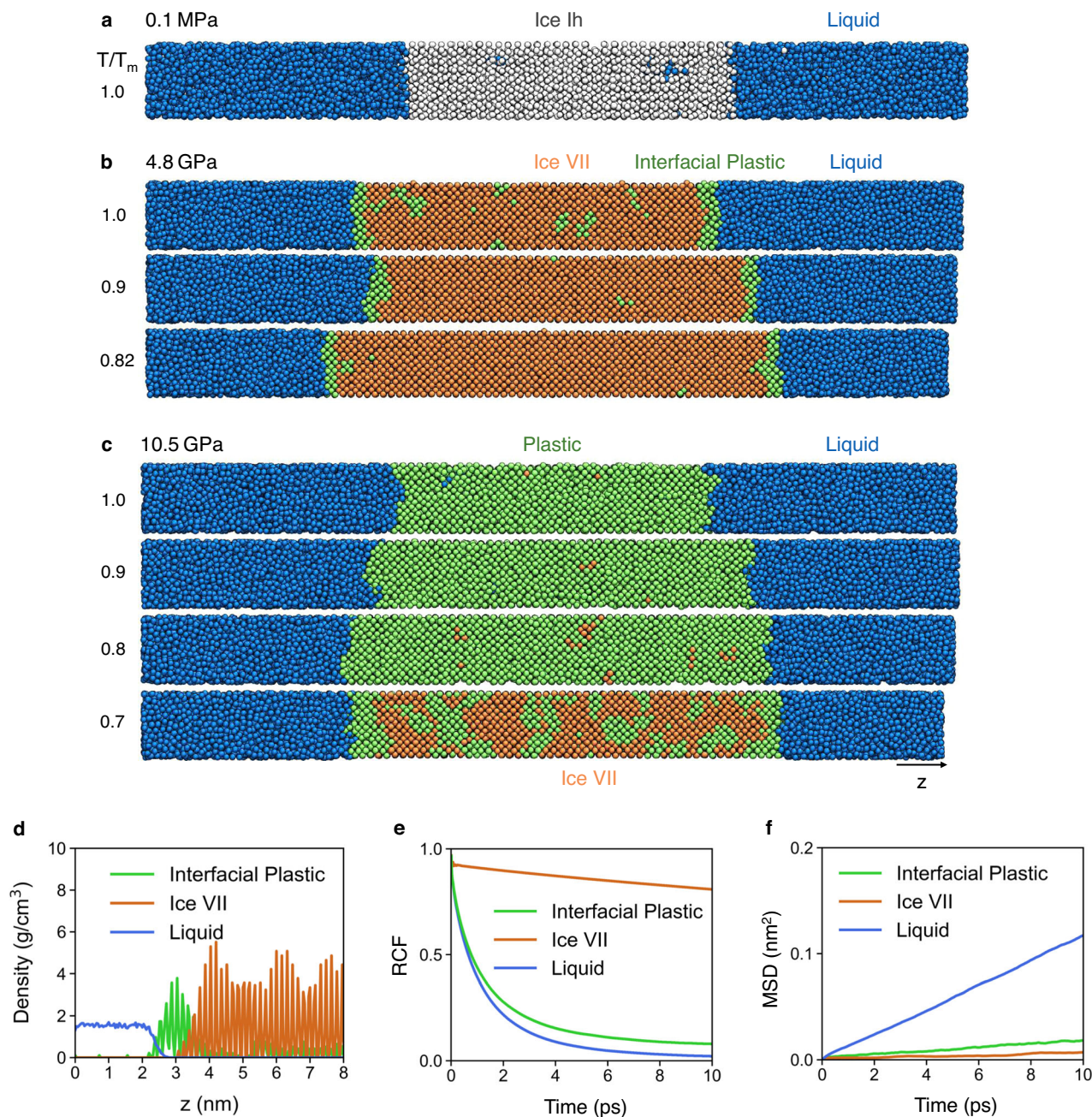


**Fig. 3** Crystal-liquid coexistence structures coloured according to the clustering using the unsupervised machine learning approach. **a-c** The crystal-liquid coexistence structures for ice Ih, ice VII, and plastic ice at varying temperatures. **d** The  $z$ -dependent density profile in the vicinity of the ice VII-liquid interface at  $T_m$  and 4.8 GPa. Dynamical features, **e** reorientational correlation function (RCF) and **f** mean square displacement (MSD), for water molecules in each cluster of ice VII-liquid coexistence at the melting temperature ( $T_m$ ).

stepwise decrease in the Voronoi volume can be seen, although it largely fluctuates, consistent with the change of cluster type. In both transitions, from liquid to interfacial plastic and from interfacial plastic to ice VII, the variation appears not gradual but distinct. Accordingly, although the growth rate of ice VII largely deviates from the WF prediction, the one-by-one freezing supposed in the WF model describes the molecular picture more accurately than the gradual density variation expected in the wave-propagation scenario of the collision-controlled model.

Which process dominates the growth of ice VII from the liquid? To answer this question, we build a coexistence between ice VII and plastic ice and relax it at 383 K ( $0.9T_m$  for ice VII) and 4.8 GPa. (see Methods section for details). Figure 4b shows the

time evolution of the number of ice VII molecules. As can be seen in the insets of Fig. 4b, spinodal decomposition occurs in many places at 20 ps because plastic ice under this thermodynamic condition is extremely unstable. However, the sole advance of ice VII crystal front is observed, albeit briefly, during the period from 0 to 10 ps (Supplementary Fig. 9). A linear fitting to that period, combined with Eq. (4), estimates the growth rate as 130 m/s, which is much faster than that of ice VII from liquid (at most 31 m/s). Thus, the transition from liquid to interfacial plastic layer, rather than from interfacial plastic layer to ice VII, primarily controls the overall growth rate of ice VII from liquid.

The temperature dependence of the interfacial domain width is examined. Figure 4c shows the fraction of each cluster as a function

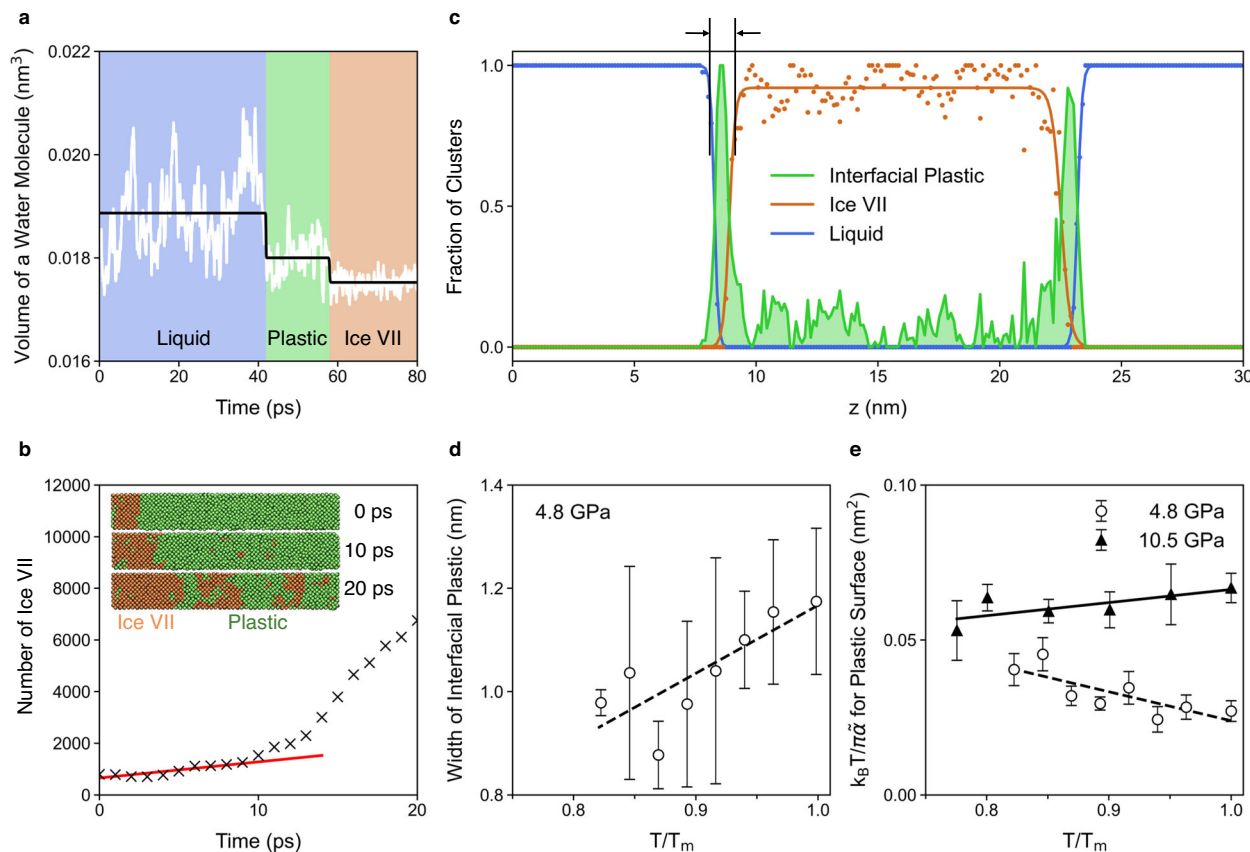


**Fig. 4 Properties of the interfacial plastic domain.** **a** Voronoi volume of a typical water molecule at the instant when it is incorporated into ice VII ( $T/T_m=0.9$  and 4.8 GPa).  $T_m$  is the melting temperature. White and black lines, respectively, show the running average over 0.4 ps (40 points) and sigmoidal-curve fitting. The colour slabs represent the clusters to which the molecule belongs. **b** Number of ice VII molecules vs. time for the coexistence between ice VII and plastic ice ( $T/T_m=0.9$  and 4.8 GPa). The red line is a linear fitting of the period between 0 and 10 ps. The insets depict a part of the coexistence system, in which orange and green particles represent ice VII and plastic ice crystals. **c**  $z$  dependence of the fraction of clusters for a typical snapshot of ice VII–liquid coexistence, with sigmoidal functions (solid lines) fitting the ice VII and liquid fractions (dots). The black solid lines and arrows indicate the width of interfacial plastic region. Temperature dependence of **d** the width of interfacial plastic domain at 4.8 GPa and **e** the roughness  $k_B T / \pi \tilde{\alpha}$  for the surface between (interfacial) plastic ice and liquid at 4.8 GPa and 10.5 GPa.

of  $z$  for a crystal–liquid configuration at  $T_m$  of 4.8 GPa. As expected, the plastic ice fraction exhibits a pronounced peak at the interface between ice VII and liquid. A small portion of the plastic particles is also observed in bulk ice VII (13 % at  $T_m$ ), which tends to disappear with cooling. The curves for ice VII and liquid fractions are fitted using a sigmoid function, and their 90% drop is used to define the width of the interfacial domain. Figure 4d shows that the width of the interfacial domain is reduced upon cooling. As demonstrated for colloids and metals, pre-ordering plays a key role in fast crystal growth, where only a small adjustment is required for the transition to the crystal<sup>1,2</sup>. If we define the activation energy for crystallisation as  $E_a = -k_B \partial \ln K / \partial (1/T)$ ,  $E_a$  (computed from Fig. 1h) increases upon cooling, indicating that the transition from liquid to ice VII becomes more difficult. Thus, regarding the interfacial plastic region as the pre-ordering of ice VII, the increases in  $E_a$  may arise from the reduction of the pre-ordering layer.

We also characterise the surface roughness by the height correlation function<sup>25,44–46</sup>

$$G(r) = \langle [h(\mathbf{r}) - h(\mathbf{0})]^2 \rangle, \quad (3)$$

where  $h$  is the height at  $\mathbf{r} = (x, y)$  on the lateral plane.  $\langle \dots \rangle$  is an ensemble average that runs over the sampled snapshots and the position of the origin  $\mathbf{0}$ .  $G$  diverges logarithmically as  $k_B T / \pi \tilde{\alpha} \ln(r/d)$  for a rough surface, where  $\tilde{\alpha}$  is a surface stiffness,

whereas  $G$  saturates for a faceted surface<sup>45</sup>. The surface is defined as the oxygen atoms in the plastic domain that are accessible from the liquid domain using a spherical probe with a radius of 0.2 nm<sup>47</sup>. We perform MD simulations for a more extensive system than that of  $V_n$  and find that  $G(r)$  diverges with  $r$  for all the configurations examined, thus indicating a rough surface (Supplementary Fig. 10).  $k_B T / \pi \tilde{\alpha}$  is then obtained from a linear fitting to the semi-log plot of  $G(r)$ . Analogous to the correlation between the step stiffness and the density of kinks on a surface and thus also with the fraction of favourable growth sites ( $f$ ) in the WF model. Figure 4e shows that  $k_B T / \pi \tilde{\alpha}$  increases upon cooling in the case of the plastic–liquid surface on ice VII at 4.8 GPa, whereas it remains relatively stable for the plastic–liquid surface at 10.5 GPa. In other words, the plastic–liquid surface becomes rougher; thus,  $f$  increases upon cooling at 4.8 GPa, but not at 10.5 GPa. Assuming  $E_a$  is a constant, the increase in  $f$  results in the deviation of  $\ln K$  from a linear function of  $1/T$ , as observed in Fig. 1h. Further studies are required to clarify whether  $E_a$ ,  $f$ , or a combination of the two, is associated with the non-linear dependence of  $\ln K$  on  $1/T$  for the melt growth of ice VII.

**Difference between ice VII and plastic ice.** Using a simple model, we establish that the greatly distorted bcc-lattice structure (representative of plastic ice) is distinguishable from the

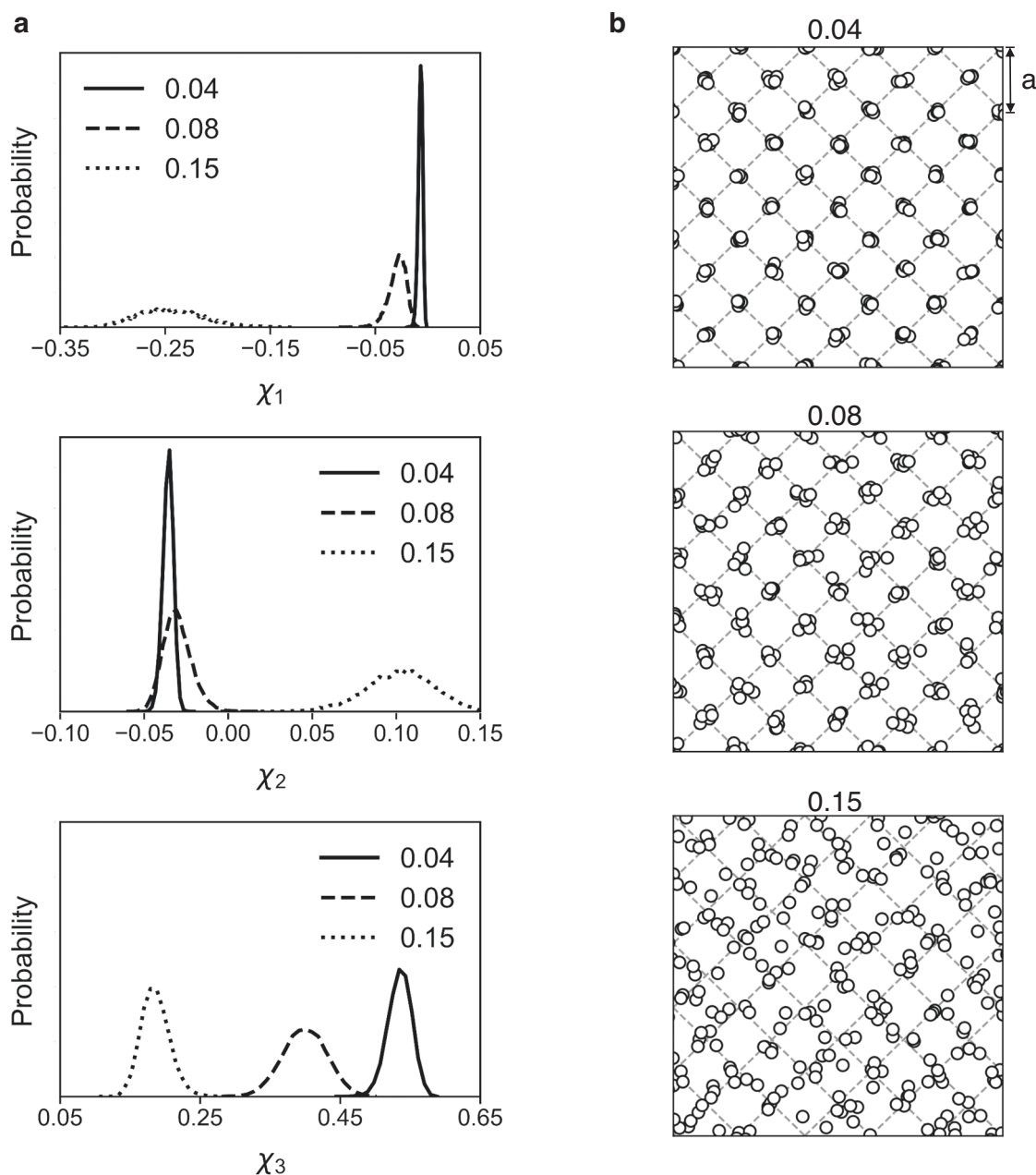


**Fig. 5 Influence of the lattice distortion in the model bcc crystal composed of independent harmonic oscillators on identifying the local structural environments.** **a** Probability distribution of the distorted bcc-lattice with  $\sigma/a=0.04, 0.08$ , and  $0.15$  on the  $\chi_1$ - $\chi_2$ - $\chi_3$  subspace.  $\sigma$  is the standard deviation of particle position around a lattice site;  $a$  is the lattice constant of bcc-lattice;  $\chi_1, \chi_2, \chi_3$  are the three-dimensional nonlinear projection of the original input vectors. **b** Schematic description for those distortions. The dashed lines in grey are for the eye guide.

moderately distorted bcc-lattice structure (representative of ice VII) within our methodology. We assume that the model bcc-lattice contains a large number of independent three-dimensional harmonic oscillators of the same spring constant  $c$ . The particle position around a lattice site ( $\Delta r$ ) follows the Gaussian distribution ( $\propto \exp(-\Delta r^2/2\sigma^2)$ ) with the standard deviation  $\sigma = \sqrt{k_B T/c}$ . The distorted bcc-lattice of 16000 particles is generated by the pycsal package, and the resulting local environment is projected on the  $\chi_1 - \chi_2 - \chi_3$  subspace. In Fig. 5a, the distributions with  $\sigma/a = 0.04, 0.08$ , and  $0.15$  ( $a$  is the lattice constant and the cut-off for neighbours is  $1.14a$ ) reproduce reasonably well the distributions for ice VII, plastic ice, and liquid in Fig. 2c, respectively. Figure 5b provides a schematic representation of these deviations. These findings bring evidence that the degree of distortion present in the bcc lattice differs between ice VII and plastic ice.

## Conclusions

In summary, the results of our study have suggested that ice VII and plastic ice grow outstandingly faster than ice Ih, which significantly exceeds the growth rate expected from the classical WF model. The discovered fast growth rate of ice VII, which maintains a specific hydrogen bond network, was attributed to the decoupling of translational and orientational ordering occurring through an interfacial plastic layer. The accelerated growth kinetics associated with the globular molecular features in the plastic phase is consistent with the computational observation that the monoatomic water model, due to the absence of hydrogen, overestimates the growth rate of ice Ih by order of magnitude of 2 to 3 compared to the all-atom models<sup>10</sup>. The bcc-like local structure of high-density water may also impact the fast local ordering of the plastic ice (layer)<sup>48,49</sup>.



The classification of each molecule into relevant local molecular environments provided further details on how liquid molecule freezes into ice VII. More specifically, we found that (i) the crystal front advances via distinct transitions of each molecule, (ii) the incorporation from liquid to interfacial plastic layer dominates the overall growth rate, and (iii) the width and roughness of the interfacial domain correlates with the growth kinetics. Furthermore, although many studies have focused on the growth front and nearby liquid in order to rationalise the molecular mechanism of fast growth, the observed remarkably high growth rate for plastic ice suggests that the nature of bulk crystal itself—in our case, it is orientational disordering—also plays an essential role in determining the growth mode.

Our numerical approach of the fine combination of MD simulations with UML is directly applicable to other high-pressure ice crystals, e.g., to study the role of high-density liquid layer found on ice III and ice VI<sup>50</sup>, as well as the structural changes in hydration shell which support the functions of macromolecules<sup>51–53</sup>. Because UML does not require supervision—this differs from supervised machine learning, where one would need to assume that the structures are known, i.e., labelled by the expert—it can detect unknown ice structures as long as the data is of sufficient amount and quality and that the descriptors are relevant and informative about those structures.

Ice VII occurs under extreme environments, such as the Earth's deep mantle and extraterrestrial space<sup>54,55</sup>. However, recent studies predicted ice VII-like structures even at ambient conditions in nanospaces between metal nanoparticles<sup>56</sup> or polymers<sup>57</sup>. More generally, a plastic (or rotator) phase is not limited to water<sup>58–60</sup>. Thus, our findings would provide a better understanding of the melt growth mechanism of various materials and offer a guide for producing high-quality crystallines. The potential formation of an orientationally disordered wetting layer would be important information when we examine the binding mechanism of additives to crystals (e.g., antifreeze proteins)<sup>61</sup> or chemical reactions on crystals<sup>62</sup>.

## Methods

**MD simulations.** MD simulations are performed using the GROMACS 2020.6 package<sup>63</sup>. Water molecules are represented by the TIP5P rigid water model<sup>64</sup>. In this model, bcc-plastic ice, in which oxygen atoms adopt a bcc lattice, forms from ice VII via the first order phase transition upon heating at several gigapascals<sup>30,42,65</sup>. Although several different types of plastic ice crystals exist<sup>66,67</sup>, plastic ice in this study represents the bcc form of plastic ice.

TIP4P series have been widely used for studying phase transitions of water<sup>68–70</sup>. However, the TIP5P model more closely reproduces the experimental densities of ice VII when compared to the TIP4P/2005 model<sup>71</sup>. Naturally-occurring ice VII becomes the most stable ice polymorphs at pressures greater than 2 GPa. In contrast, ice VII in the TIP4P/2005 model and the SPC/E model exhibits stability at pressures exceeding 10 GPa, and hypothetical ice crystals (not existing in nature) become stable at lower pressures<sup>66</sup>. Moreover, ice VII in the TIP4P/2005 model transforms into plastic ice at higher temperatures when the pressure is greater than 4 GPa<sup>72</sup> or 6 GPa<sup>31</sup>. Thus, ice VII in the TIP4P/2005 model would not be a stable phase at any pressure on the solid-liquid coexistence boundary in the phase diagram. Other models in the TIP4P series, such as TIP4P and TIP4P/Ice, would display comparable phase behaviours as TIP4P/2005 since they are known to primarily shift the temperature of the phase diagram<sup>73,74</sup>. Although a hypothetical ice crystal also exists between ice VI and ice VII on the phase diagram of the TIP5P model, the pressure at which ice VII becomes stable (>4 GPa) is considerably lower than that observed in the TIP4P/2005 and SPC/E models (>10 GPa)<sup>66</sup>. Furthermore, attempts to forcibly grow metastable ice VII in the TIP4P/2005 model have been observed to result in the appearance of a hypothetical ice crystal on the ice VII surface, thereby precluding measurements of ice VII growth rate<sup>75</sup>. In contrast, the TIP5P model allows for the measurement of the growth rate of both ice VII and plastic ice, as shown below.

The pair interactions are truncated at 0.9 nm. Long-range dispersion corrections are applied to energy and pressure, and long-range Coulombic interactions are evaluated using the particle-mesh Ewald algorithm. Periodic boundary conditions are applied in all directions. The equation of motion is integrated with the leapfrog algorithm using a time step of 2 fs. In the equilibrations, the temperature  $T$  and pressure  $p$  are controlled using the Berendsen algorithm with a damping constant of 20 ps (1.0 ps for 0.1 MPa), while the Nosé–

Hoover thermostat with a damping constant of 2.0 ps is used for  $T$  in the production runs.

The growth rate of a planar ice surface is measured using crystal–liquid systems in an elongated box with dimensions of approximately  $2.7 \times 2.9 \times 48.4$  nm for ice Ih and  $2.6 \times 2.6 \times 32.2$  nm for ice VII and plastic ice. The total number of molecules  $N$  is 12288. The primary prismatic surface of ice Ih and the {100} surface of ice VII and plastic ice are exposed in the  $z$ -direction. The structures of ice Ih and ice VII are generated using the GenIce package<sup>76</sup>. Then, 80% of the crystal is melted at a high temperature by applying position restraints to the remaining part. Plastic ice spontaneously forms from ice VII when  $T$  and  $p$  are increased.

MD simulations are carried out under the isothermal–isobaric ( $NpT$ ) ensemble. Ice Ih, ice VII, and plastic ice under 0.1 MPa, 4.8 GPa, and 10.5 GPa, respectively, are considered. Semi-isotropic pressure coupling is used for crystal–liquid systems, in which the pressure coupling is isotropic in  $x$ - and  $y$ -directions but different in  $z$ -direction. Thus, the volume change due to crystallisation results in a change in the  $z$ -direction of the simulation cell. Three independent trajectories are generated from two different initial structures; thus, the growth rate for each condition is estimated from six trajectories.

The normal growth rate  $V_n$  is computed as follows:

$$V_n = \frac{\Delta N_{\text{ice}}}{2\Delta t} \times \frac{L_z}{N}, \quad (4)$$

where  $\Delta N_{\text{ice}}/\Delta t$  is the slope of a linear fitting to the time ( $t$ ) evolution of the number of ice-like molecules ( $N_{\text{ice}}$ ), and  $L_z$  is the box length along the  $z$ -axis when the entire system is frozen. For ice VII and plastic ice, ice-like molecules are defined by  $\bar{q}_6 > 0.25$ , while that for ice Ih is set as  $\bar{q}_6 > 0.40$  ( $\bar{q}_6$  is explained below). Half of the slope is associated with a single growth front because melt growth occurs at both ends of the crystal. In the same manner, we also compute the negative growth rate (i.e., for melting) and estimate the melting temperature ( $T_m$ ) using the framework of the direct coexistence method (Supplementary Fig. 11)<sup>77</sup>. The obtained  $T_m$ s are summarised in Table 1.

To estimate the growth rate of ice VII from plastic ice, we transform 90% of ice VII to plastic ice by performing MD simulations under canonical ensemble at 800 K with applying position constraints to the remaining part. Using the resulting coexistence as the initial structure (Supplementary Fig. 9a), we perform 100 ps simulation at 383 K (0.9  $T_m$  for ice VII) and 4.8 GPa. Ice VII and plastic ice are identified by the UML approach. The  $\Delta N_{\text{ice}}/\Delta t$  is computed by a linear fitting from 0 to 10 ps, during which the sole advance of ice VII crystal front is observed (Supplementary Fig. 9). By applying Eq. (4), the growth rate of ice VII from plastic ice is determined.

Enthalpies, diffusion coefficients, rotational correlation functions, and radial distribution functions for bulk configurations are computed using 5488 water molecules in a nearly cubic box, in which the pressure is isotropically controlled. For each condition, a 1 ns equilibration run is followed by a production run for several dozens of ns. In addition, a larger system of  $12.7 \times 12.7 \times 32.7$  nm, comprising 307,200 molecules, is used to compute the height correlation function of the ice surface.

**Structural characterisation.** The local structure around  $i$ -th particle is characterised by the average version of bond orientational order parameter  $\bar{q}_l(i)$  with the spherical harmonics of order  $l$ <sup>78</sup>. We focus only on the coordinates of oxygen atoms.

$$\bar{q}_l(i) = \sqrt{\frac{4\pi}{2l+1} \sum_{m=-l}^l |\bar{q}_{lm}(i)|^2}, \quad (5)$$

where

$$\bar{q}_{lm}(i) = \frac{1}{N_b(i)+1} \left[ q_{lm}(i) + \sum_{k \in N_b(i)} q_{lm}(k) \right]$$

and

$$q_{lm}(i) = \frac{1}{N_b(i)} \sum_{j \in N_b(i)} Y_l^m(\mathbf{r}_{ij}). \quad (6)$$

$\tilde{N}_b(i)$  is the set of nearest neighbours of  $i$ -th particle within a cutoff of 0.35 nm for 0.1 MPa and 0.40 nm for the other pressures.  $\tilde{N}_b(i)$  contains  $N_b(i)$  particles.  $Y_l^m(\mathbf{r}_{ij})$  are the spherical harmonics of order  $l$  with an integer  $m$  ranging from  $m = -l$  to  $m = +l$ .  $\mathbf{r}_{ij}$  extends from  $i$ -th particle to  $j$ -th particle. Then, the local structural environment of  $i$ -th particle is represented by a six-dimensional vector:

$$\mathbf{Q}(i) = (\bar{q}_2(i), \bar{q}_4(i), \bar{q}_6(i), \bar{q}_8(i), \bar{q}_{10}(i), \bar{q}_{12}(i)). \quad (7)$$

Following the work by Boattini et al.<sup>35,36</sup>, we apply a UML approach to group similar local environments. A neural network-based autoencoder is trained to perform the input reconstruction task through a low-dimensional nonlinear projection that preserves the most relevant features of the data. The input data is the sum of the vectors  $\mathbf{Q}(i)$  obtained from MD simulations for crystal–liquid coexistence systems. The network layers in the encoder and decoder structures are taken from PyTorch (Python package)<sup>79</sup>. We use one hidden layer of dimension 60 for both the encoder and the decoder parts of the network. A hyperbolic tangent

activation function is applied between the linear layers of the autoencoder for non-linear mapping.

To prevent potential overfitting and to improve the robustness to small variations in the input data, we use a ridge regression approach<sup>80</sup>. This approach minimises the mean square errors plus a fraction of the L2 norm of the model's weight vector<sup>38</sup>. The corresponding cost function can be expressed as follows:

$$\frac{1}{N_s} \sum_{i=1}^{N_s} \|\mathbf{Q}(i) - \hat{\mathbf{Q}}(i)\|^2 + \phi \sum_{j=1}^M w_j^2, \quad (8)$$

where  $N_s$  is the number of input vectors,  $\hat{\mathbf{Q}}(i)$  is the output vector of  $i$ -th particle,  $M$  is the total number of weights  $w_j$ , and  $\phi$  is set to  $10^{-535}$ .  $M$  is automatically determined in the autoencoder. The cost function is minimised using a minibatch stochastic gradient descent with momentum<sup>81</sup>.

Similar environments in the determined low-dimensional subspace are grouped together by a GMM. The main assumption of GMM is that the data is generated from a mixture of Gaussian distributions with unknown parameters. We learn the parameters using the expectation-maximisation algorithm available in the scikit-learn library in Python<sup>82</sup>. The optimal number of clusters is determined by finding an elbow on the BIC using the L-method<sup>39</sup>.

## Data availability

The authors declare that the data supporting the findings of this study are available within the paper and its Supplementary Information files (pdf and Movie).

## Code availability

If you have any questions or need further clarification regarding the code, please feel free to reach out to the authors at [kenji\\_mochizuki@zju.edu.cn](mailto:kenji_mochizuki@zju.edu.cn).

Received: 13 February 2023; Accepted: 22 June 2023;

Published online: 04 July 2023

## References

- Gao, Q. et al. Fast crystal growth at ultra-low temperatures. *Nat. Mater.* **20**, 1431–1439 (2021).
- Sun, G., Xu, J. & Harrowell, P. The mechanism of the ultrafast crystal growth of pure metals from their melts. *Nat. Mater.* **17**, 881–886 (2018).
- Salzmann, C. G. Advances in the experimental exploration of water's phase diagram. *J. Chem. Phys.* **150**, 060901 (2019).
- Millot, M. et al. Nanosecond x-ray diffraction of shock-compressed superionic water ice. *Nature* **569**, 251–255 (2019).
- Gasser, T. M., Thoeny, A. V., Fortes, A. D. & Loerting, T. Structural characterization of ice xix as the second polymorph related to ice vi. *Nat. Commun.* **12**, 1128 (2021).
- Yamane, R. et al. Experimental evidence for the existence of a second partially-ordered phase of ice vi. *Nat. Commun.* **12**, 1129 (2021).
- Engel, E. A., Anelli, A., Ceriotti, M., Pickard, C. J. & Needs, R. J. Mapping uncharted territory in ice from zeolite networks to ice structures. *Nat. Commun.* **9**, 2173 (2018).
- Mochizuki, K., Himoto, K. & Matsumoto, M. Diversity of transition pathways in the course of crystallization into ice VII. *Phys. Chem. Chem. Phys.* **16**, 16419–16425 (2014).
- Petrenko, V. & Whitworth, R. *Physics of Ice* (OUP Oxford, 1999).
- Espinosa, J. R., Navarro, C., Sanz, E., Valeriani, C. & Vega, C. On the time required to freeze water. *J. Chem. Phys.* **145**, 211922 (2016).
- Pruppacher, H. R. Interpretation of experimentally determined growth rates of ice crystals in supercooled water. *J. Chem. Phys.* **47**, 1807–1813 (1967).
- Razul, M. G. & Kusalik, P. Crystal growth investigations of ice/water interfaces from molecular dynamics simulations: profile functions and average properties. *J. Chem. Phys.* **134**, 014710 (2011).
- Gleason, A. E. et al. Compression freezing kinetics of water to ice VII. *Phys. Rev. Lett.* **119**, 025701 (2017).
- Dolan, D., Knudson, M., Hall, C. & Deeney, C. A metastable limit for compressed liquid water. *Nat. Phys.* **3**, 339–342 (2007).
- Bastea, M., Bastea, S., Reaugh, J. E. & Reisman, D. B. Freezing kinetics in overcompressed water. *Phys. Rev. B* **75**, 172104 (2007).
- Myint, P. C. & Belof, J. L. Rapid freezing of water under dynamic compression. *J. Phys.: Condens. Matter* **30**, 233002 (2018).
- Jackson, K. A. The interface kinetics of crystal growth processes. *Interface Sci.* **10**, 159–169 (2002).
- Chernov, A. A. Notes on interface growth kinetics 50 years after burton, cabrera and frank. *J. Cryst. Growth* **264**, 499–518 (2004).
- Hu, Y.-C. & Tanaka, H. Revealing the role of liquid preordering in crystallisation of supercooled liquids. *Nat. Commun.* **13**, 1–12 (2022).
- Wilson, H. W. On the velocity of solidification and viscosity of super-cooled liquids. *Philos. Mag.* **50**, 238–250 (1900).
- Frenkel, J. *Kinetic Theory of Liquids* (Oxford University Press, 1946).
- Ediger, M. D., Harrowell, P. & Yu, L. Crystal growth kinetics exhibit a fragility-dependent decoupling from viscosity. *J. Chem. Phys.* **128**, 034709 (2008).
- Grabow, M. H., Gilmer, G. H. & Bakker, A. F. Molecular dynamics studies of silicon solidification and melting. *Mater. Res. Soc. Symp. Proc.* **141**, 349–354 (1989).
- Rozmanov, D. & Kusalik, P. G. Anisotropy in the crystal growth of hexagonal ice, ih. *J. Chem. Phys.* **137**, 094702 (2012).
- Mochizuki, K., Murata, K.-i & Zhang, X. Microscopic ordering of supercooled water on the ice basal face. *Commun. Mater.* **4**, 33 (2023).
- Ashkenazy, Y. & Averbach, R. S. Kinetic stages in the crystallization of deeply undercooled body-centered-cubic and face-centered-cubic metals. *Acta Mater.* **58**, 524–530 (2010).
- Broughton, J. Q., Gilmer, G. H. & Jackson, K. A. Crystallization rates of a Lennard-Jones liquid. *Phys. Rev. Lett.* **49**, 1496–1500 (1982).
- Hawken, A., Sun, G. & Harrowell, P. Role of interfacial inherent structures in the fast crystal growth from molten salts and metals. *Phys. Rev. Mater.* **3**, 043401 (2019).
- Wang, L., Hu, L., Zhao, J. F. & Wei, B. Ultrafast growth kinetics of titanium dendrites investigated by electrostatic levitation experiments and molecular dynamics simulations. *Chem. Phys. Lett.* **742**, 137141 (2020).
- Takii, Y., Koga, K. & Tanaka, H. A plastic phase of water from computer simulation. *J. Chem. Phys.* **128**, 204501 (2008).
- Aragones, J. L. & Vega, C. Plastic crystal phases of simple water models. *J. Chem. Phys.* **130**, 244504 (2009).
- Adachi, Y. & Koga, K. Structure and phase behavior of high-density ice from molecular-dynamics simulations with the ReaxFF potential. *J. Chem. Phys.* **153**, 114501 (2020).
- García Fernández, R., Abascal, J. L. & Vega, C. The melting point of ice ih for common water models calculated from direct coexistence of the solid-liquid interface. *J. Chem. Phys.* **124**, 144506 (2006).
- Zimón, M. J. & Martelli, F. Molecular rotations trigger a glass-to-plastic fcc heterogeneous crystallization in high-pressure water. *J. Chem. Phys.* **158**, 114501 (2023).
- Boattini, E., Dijkstra, M. & Filion, L. Unsupervised learning for local structure detection in colloidal systems. *J. Chem. Phys.* **151**, 154901 (2019).
- Boattini, E. et al. Autonomously revealing hidden local structures in supercooled liquids. *Nat. Commun.* **11**, 5479 (2020).
- Lechner, W. & Dellago, C. Accurate determination of crystal structures based on averaged local bond order parameters. *J. Chem. Phys.* **129**, 114707 (2008).
- Bishop, C. M. et al. *Neural Networks for Pattern Recognition* (Oxford University Press, 1995).
- Salvador, S. & Chan, P. Determining the number of clusters/segments in hierarchical clustering/segmentation algorithms. In *16th IEEE International Conference on Tools with Artificial Intelligence* 576–584 (IEEE, 2004).
- Olden, J. D., Joy, M. K. & Death, R. G. An accurate comparison of methods for quantifying variable importance in artificial neural networks using simulated data. *Ecol. Modell.* **178**, 389–397 (2004).
- Yao, J., Teng, N., Poh, H.-L. & Tan, C. L. Forecasting and analysis of marketing data using neural networks. *J. Inf. Sci. Eng.* **14**, 843–862 (1998).
- Himoto, K., Matsumoto, M. & Tanaka, H. Yet another criticality of water. *Phys. Chem. Chem. Phys.* **16**, 5081–5087 (2014).
- Nagata, Y. et al. The surface of ice under equilibrium and nonequilibrium conditions. *Acc. Chem. Res.* **52**, 1006–1015 (2019).
- Berrens, M. L., Bononi, F. C. & Donadio, D. Effect of sodium chloride adsorption on the surface premelting of ice. *Phys. Chem. Chem. Phys.* **24**, 20932–20940 (2022).
- Saito, Y. *Statistical Physics of Crystal Growth* (World Scientific, 1996).
- Benet, J., Llobart, P., Sanz, E. & MacDowell, L. G. Premelting-induced smoothening of the ice-vapor interface. *Phys. Rev. Lett.* **117**, 096101 (2016).
- Sega, M., Hantal, G., Fábán, B. & Jedlovský, P. Pytim: a python package for the interfacial analysis of molecular simulations. *J. Comput. Chem.* **39**, 2118–2125 (2018).
- Lee, G. W., Evans, W. J. & Yoo, C.-S. Crystallization of water in a dynamic diamond-anvil cell: evidence for ice vii-like local order in supercompressed water. *Phys. Rev. B* **74**, 134112 (2006).
- Saitta, A. M. & Datchi, F. Structure and phase diagram of high-density water: the role of interstitial molecules. *Phys. Rev. E* **67**, 020201 (2003).
- Niinomi, H. et al. High-density liquid water at a water-ice interface. *J. Phys. Chem. Lett.* **11**, 6779–6784 (2020).
- Mochizuki, K. & Ben-Amotz, D. Hydration-Shell transformation of thermosensitive aqueous polymers. *J. Phys. Chem. Lett.* **8**, 1360–1364 (2017).

52. Zhou, D., Wan, L.-S., Xu, Z.-K. & Mochizuki, K. Less-ordered hydration shell around poly(N,N-diethylacrylamide) is insensitive to the clouding transition. *J. Phys. Chem. B* **125**, 12104–12109 (2021).
53. Laage, D., Elsaesser, T. & Hynes, J. T. Water dynamics in the hydration shells of biomolecules. *Chem. Rev.* **117**, 10694–10725 (2017).
54. Tschauer, O. et al. Ice-VII inclusions in diamonds: evidence for aqueous fluid in earth's deep mantle. *Science* **359**, 1136–1139 (2018).
55. Bina, C. R. & Navrotsky, A. Possible presence of high-pressure ice in cold subducting slabs. *Nature* **408**, 844–847 (2000).
56. Shin, D., Hwang, J. & Jhe, W. Ice-VII-like molecular structure of ambient water nanomeniscus. *Nat. Commun.* **10**, 286 (2019).
57. Yamazoe, K. et al. Enhancement of the hydrogen-bonding network of water confined in a polyelectrolyte brush. *Langmuir* **33**, 3954–3959 (2017).
58. Personage, N. & Stevelly, L. *Disorder in Crystals* (Oxford University, 1978).
59. Timmermans, J. Plastic crystals: a historical review. *J. Phys. Chem. Solids* **18**, 1–8 (1961).
60. Zhang, H. et al. Observation of a plastic crystal in water–ammonia mixtures under high pressure and temperature. *J. Phys. Chem. Lett.* **14**, 2301–2307 (2023).
61. Hudait, A. et al. Preordering of water is not needed for ice recognition by hyperactive antifreeze proteins. *Proc. Natl Acad. Sci. USA* **115**, 8266–8271 (2018).
62. Watanabe, N. & Kouchi, A. Ice surface reactions: a key to chemical evolution in space. *Prog. Surf. Sci.* **83**, 439–489 (2008).
63. Hess, B., Kutzner, C., van der Spoel, D. & Lindahl, E. Gromacs 4: algorithms for highly efficient, load-balanced, and scalable molecular simulation. *J. Chem. Theory Comput.* **4**, 435–447 (2008).
64. Mahoney, M. W. & Jorgensen, W. L. A five-site model for liquid water and the reproduction of the density anomaly by rigid, nonpolarizable potential functions. *J. Chem. Phys.* **112**, 8910–8922 (2000).
65. Hernandez, J.-A. & Caracas, R. Proton dynamics and the phase diagram of dense water ice. *J. Chem. Phys.* **148**, 214501 (2018).
66. Yagasaki, T., Matsumoto, M. & Tanaka, H. Phase diagrams of TIP4P/2005, SPC/E, and TIP5P water at high pressure. *J. Phys. Chem. B* **122**, 7718–7725 (2018).
67. Henaio, A., Salazar-Rios, J. M., Guardia, E. & Pardo, L. C. Structure and dynamics of water plastic crystals from computer simulations. *J. Chem. Phys.* **154**, 104501 (2021).
68. Mochizuki, K., Matsumoto, M. & Ohmine, I. Defect pair separation as the controlling step in homogeneous ice melting. *Nature* **498**, 350–354 (2013).
69. Mochizuki, K. & Koga, K. Solid–liquid critical behavior of water in nanopores. *Proc. Natl Acad. Sci. USA* **112**, 8221–8226 (2015).
70. Mochizuki, K. & Molinero, V. Antifreeze glycoproteins bind reversibly to ice via hydrophobic groups. *J. Am. Chem. Soc.* **140**, 4803–4811 (2018).
71. Aragonés, J., Conde, M., Noya, E. & Vega, C. The phase diagram of water at high pressures as obtained by computer simulations of the tip4p/2005 model: the appearance of a plastic crystal phase. *Phys. Chem. Chem. Phys.* **11**, 543–555 (2009).
72. Toffano, A. et al. Temperature- and pressure-dependence of the hydrogen bond network in plastic ice vii. *J. Chem. Phys.* **157**, 094502 (2022).
73. Vega, C., Abascal, J., Sanz, E., MacDowell, L. & McBride, C. Can simple models describe the phase diagram of water? *J. Phys. Condens. Matter* **17**, S3283 (2005).
74. Vega, C. & Abascal, J. L. Simulating water with rigid non-polarizable models: a general perspective. *Phys. Chem. Chem. Phys.* **13**, 19663–19688 (2011).
75. Hirata, M., Yagasaki, T., Matsumoto, M. & Tanaka, H. Phase diagram of tip4p/2005 water at high pressure. *Langmuir* **33**, 11561–11569 (2017).
76. Matsumoto, M., Yagasaki, T. & Tanaka, H. GenIce: hydrogen-disordered ice generator. *J. Comput. Chem.* **39**, 61–64 (2018).
77. Ladd, A. & Woodcock, L. Triple-point coexistence properties of the Lennard-Jones system. *Chem. Phys. Lett.* **51**, 155–159 (1977).
78. Lechner, W. & Dellago, C. Accurate determination of crystal structures based on averaged local bond order parameters. *J. Chem. Phys.* **129**, 114707 (2008).
79. Paszke, A. et al. Pytorch: an imperative style, high-performance deep learning library. *Adv. Neural Inf. Process. Syst.* **32**, 8024–8035 (2019).
80. Hoerl, A. E. & Kennard, R. W. Ridge regression: Biased estimation for nonorthogonal problems. *Technometrics* **12**, 55–67 (1970).
81. Kingma, D. P. & Ba, J. Adam: a method for stochastic optimization. In *3rd International Conference for Learning Representations* 1–15 (ICLR, 2015).
82. Pedregosa, F. et al. Scikit-learn: machine learning in python. *J. Mach. Learn. Res.* **12**, 2825–2830 (2011).

## Acknowledgements

This work was supported by National Natural Science Foundation of China (Grant Nos. 22250610195, 22273083, and 82273731), Start-up Foundation for Hundred-Talent Program of Zhejiang University, and the National Key Research and Development Program of China (Grant No. 2021YFC2701905).

## Author contributions

X.Z. and Y.Y. conducted MD simulations and undertook data analysis. H.L. and A.P. were responsible for the UML analyses. The manuscript was written by A.P. and K.M. The project was conceptualised and designed by K.M.

## Competing interests

The authors declare no competing interests.

## Additional information


**Supplementary information** The online version contains supplementary material available at <https://doi.org/10.1038/s42005-023-01285-y>.

**Correspondence** and requests for materials should be addressed to Andre Python or Kenji Mochizuki.

**Peer review information** *Communications Physics* thanks the anonymous reviewers for their contribution to the peer review of this work. A peer review file is available.

**Reprints and permission information** is available at <http://www.nature.com/reprints>

**Publisher's note** Springer Nature remains neutral with regard to jurisdictional claims in published maps and institutional affiliations.

 **Open Access** This article is licensed under a Creative Commons Attribution 4.0 International License, which permits use, sharing, adaptation, distribution and reproduction in any medium or format, as long as you give appropriate credit to the original author(s) and the source, provide a link to the Creative Commons licence, and indicate if changes were made. The images or other third party material in this article are included in the article's Creative Commons licence, unless indicated otherwise in a credit line to the material. If material is not included in the article's Creative Commons licence and your intended use is not permitted by statutory regulation or exceeds the permitted use, you will need to obtain permission directly from the copyright holder. To view a copy of this licence, visit <http://creativecommons.org/licenses/by/4.0/>.

© The Author(s) 2023